Click Here for Full Article

Seasonal and interannual variability in the Mozambique Channel from moored current observations

H. Ridderinkhof,[1] P. M. van der Werf,[2] J. E. Ullgren,[1] H. M. van Aken,[1] P. J. van Leeuwen,[2,3] and W. P. M. de Ruijter[2]

[1] Direct observations from an array of current meter moorings across the Mozambique Channel in the south-west Indian Ocean are presented covering a period of more than 4 years. This allows an analysis of the volume transport through the channel, including the variability on interannual and seasonal time scales. The mean volume transport over the entire observational period is 16.7 Sv poleward. Seasonal variations have a magnitude of 4.1 Sv and can be explained from the variability in the wind field over the western part of the Indian Ocean. Interannual variability has a magnitude of 8.9 Sv and is large compared to the mean. This time scale of variability could be related to variability in the Indian Ocean Dipole (IOD), showing that it forms part of the variability in the ocean-climate system of the entire Indian Ocean. By modulating the strength of the South Equatorial Current, the weakening (strengthening) tropical gyre circulation during a period of positive (negative) IOD index leads to a weakened (strengthened) southward transport through the channel, with a time lag of about a year. The relatively strong interannual variability stresses the importance of long-term direct observations.

1. Introduction

[2] Long-term direct observations on ocean currents that span more than 1–2 years are scarce. This holds even more for direct observations on parts or branches of ocean gyres or the global overturning circulation when a large number of deep sea moorings and instruments is needed to obtain reliable information over an ocean region rather than from a single location. Examples of such observational studies in the world oceans are those of the Florida Current [*Schott et al.*, 1988], Kuroshio [*Johns et al.*, 2001], Yucatan Channel [*Sheinbaum et al.*, 2002] and the Atlantic meridional overturning circulation [*Cunningham et al.*, 2007]. The reason behind the scarceness of this type of observations is obvious: the costs in terms of manpower, ship time, instrumentation etc. is relatively large and the risk of failure is serious. By far, most of the studies on variability in ocean currents therefore rely on the application of numerical models [*Stammer et al.*, 2003]. Observational studies on long-term variability in ocean currents mostly use indirect methods, like analyzing variability in ocean tracers or, more recently,

on long-term satellite observations on the sea surface height [*Nauw et al.*, 2008].

[3] Here we present such long-term direct observations on currents and volume transport in the Mozambique Channel (MC) where the circulation consists of branches of the gyre and overturning circulation in the Indian Ocean. The observations started late 2003 and form a follow up of a pilot experiment in the area that was conducted with a current meter mooring array in 2000–2001. This pilot project showed that the flow through the MC is an important part of the greater Agulhas system [*Lutjeharms*, 2006] and forms the connection between the tropical regions and the Agulhas current and thereby of the large scale gyre circulation in the southern Indian Ocean. (For a general sketch of the region see Figure 1). The time variability of the net flow through the channel appeared to be large [*Ridderinkhof and De Ruijter*, 2003] and, due to undersampling and problems in data return, estimates on the volume transport through the channel could be done only approximately. These estimates (for 1 year of observations only) showed that the volume transport oscillates remarkably regularly with values varying roughly between 20 Sv northward and 60 Sv southward and a mean value of some 14 Sv southward, which falls in the rather wide range of previous estimates that were based on hydrographic snapshots, derived indirectly [*DiMarco et al.*, 2002] or based on global ocean model simulations [*Stammer et al.*, 2003]. Another important finding was that North Atlantic Deep Water (NADW) is present at the section, with its core hugged against the continental slope of the African

[1]Department of Physical Oceanography, Royal Netherlands Institute for Sea Research, Texel, Netherlands.
[2]Institute for Marine and Atmospheric Research Utrecht, Department of Physics and Astronomy, Utrecht University, Utrecht, Netherlands.
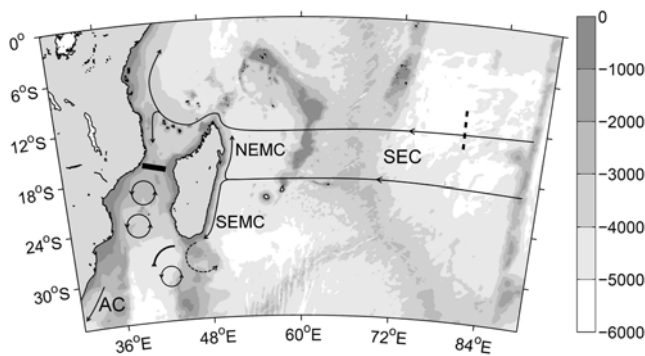[3]Department of Meteorology, University of Reading, Reading, UK.

Figure 1. Sketch of the bathymetry of the region with the main currents. The South Equatorial Current (SEC) is the main source of water in the Madagascar region. Upon reaching the islands coast, it bifurcates into the North East Madagascar Current (NEMC) and the South East Madagascar Current (SEMC). The NEMC bifurcates at the African coast, where part of the water enters the Mozambique Channel (MC). The flow in the MC mainly appears as a train of anticyclones and in the outflow region of the SEMC mainly dipole structures are found. The flow through the MC and the SEMC are both sources of the Agulhas Current (AC). The bold black line marks the mooring section, and the dashed line is the section from which the gradient of sea level anomaly was taken in order to determine the anomalous strength of the SEC.

continent. The volume transport of NADW was estimated to be about 2 Sv equatorward [*Van Aken et al.*, 2004]. This is presumably the northward extension of the Agulhas Undercurrent [*Beal and Bryden*, 1997].

[4] These exciting observations, together with our long-term interest in this ocean area [see, e.g., *De Ruijter et al.*, 1999, 2005] motivated us to setup the LOCO (Long-term Ocean Climate Observations) program, in which a mooring array has been placed in the narrows of the MC in the end of 2003. Since then, servicing and redeploying of these moorings combined with a hydrographic survey along the section has been done every 1.5–2 years. The final recovery of the moorings is now planned in 2012. Fortunately, thus far, the technical performance of the moorings and instruments has been excellent, with only very few instrument failures [*Ridderinkhof*, 2005, 2008; *Ridderinkhof and Quartly*, 2006].

[5] First analyses of the mooring data for the period from the end of 2003 to early 2006 has been presented by *Harlander et al.* [2009]. In that paper the observed time variability of the volume transport was analyzed using measurements from the first two available deployment periods covering some 2.5 years. The focus was on quantifying and analyzing the variability in the currents and volume transport at the dominant frequency of 5 to 6 per year since the currents with frequencies at this part of the spectrum appeared to dominate the temporal variability in the currents and volume transport. This frequency was found to be related both to a Rossby wave channel mode and the formation or passage of eddies at the mooring section location, suggesting a strong relation between the Rossby waves and the formation of eddies although the precise mechanism leading to the formation of these eddies could not be deduced from the observations. Other possible causes of the 5/y eddy

frequency are an oceanic connection to the equatorial region [*Schouten et al.*, 2002; *Palastanga et al.*, 2006] or baroclinic instability of the south Indian Ocean Countercurrent (SICC) [*Palastanga et al.*, 2007] that propagates westward around 24°S.

[6] In the present paper observations from the same mooring array are analyzed. As a basis for this analysis we now use observations from the period from the end of 2003 to early 2008. Thus, as compared to our previous publication on this data set [*Harlander et al.*, 2009], one additional period of about 2 years is available that nearly doubles the total length. This last 2 year period of observations was very successful in that almost all planned current measurements succeeded. The full spatial coverage of instruments during the last period allowed us to recalculate the volume transport through the channel also during the first two periods. Relations to nearby observations in the mooring array could be derived to fill data gaps (due to failing instruments or moorings) in the first two periods. Thus, estimates on the (variability in) the volume transport through the channel could be made more reliable. Moreover, the observations covering now more than 4 years made it possible to study variability at longer time scales than our previous studies. Therefore, in analyzing the results we now focus on variability at seasonal and longer (interannual) time scales. Previous studies [*De Ruijter et al.*, 2005] have shown that variability in the ocean circulation at these time scales is most presumably coupled to variability in the entire Indian Ocean. Moreover, recently *Schott et al.* [2009] have shown that the influence of the Indian Ocean on climate variability may be much stronger than previously thought, thereby expressing the importance of knowledge on the variability of the ocean circulation on these time scales.

[7] We first present the observations from the current meters at the mooring array (section 2) including the mean and standard deviation of the currents over the entire period. Then we present and discuss the use of these data to estimate the volume transport through the section. For this several inter- and extrapolations are needed. The effect of different choices is discussed focusing on its consequence on the calculated long-term variability of the volume transport (section 3). The long-term variability in the volume transport is discussed in the remainder of the paper where this variability is related to possible large scale sources of variability in the Indian Ocean like the wind field, the Indian Ocean Dipole (IOD) and the input from the Indonesian Throughflow. A comparison is made also with anomalies in the sea surface gradient across the South Equatorial Current (SEC) from satellite altimetry observations in the same time period, in order to find possible connections between the (interannual) variability in the volume transport through the MC and other branches of the gyre circulation in the southern Indian Ocean.

2. Direct Current Observations

2.1. Instrumentation and Data Return

[8] The array of seven long current meter moorings plus one short sediment trap mooring has been maintained across the narrowest part of the channel, at about 17°S, since November 2003 (Figure 1). The moorings were serviced and redeployed in March 2005, March 2006, and January 2008.
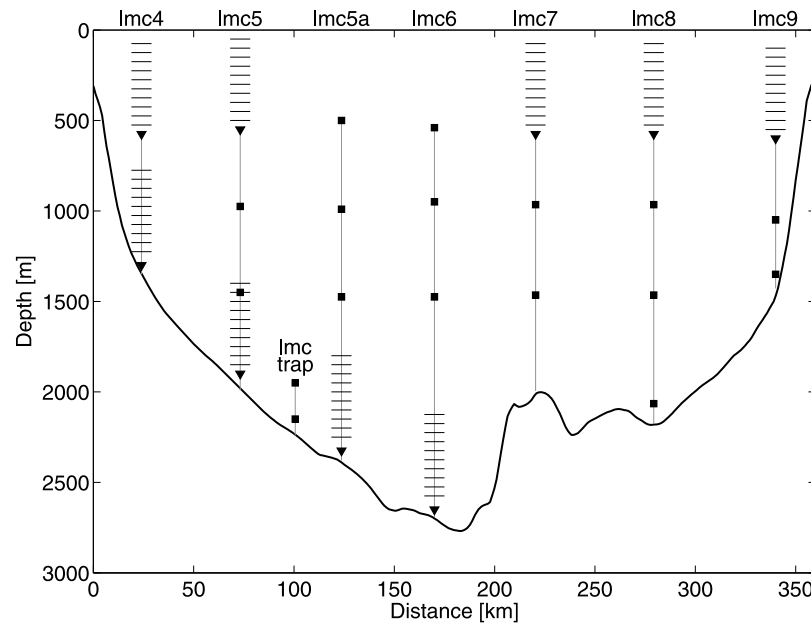
Figure 2. Design positions of current meters (squares) and ADCPs (triangles; profiling range marked by horizontal stripes). Due to instrument failures the positions of instruments returning data may differ slightly (see Table 1).

The current measurements described in this paper span the three deployment periods between November 2003 and January 2008.

[9] The mooring array was designed with upward looking Acoustic Doppler Current Profilers (ADCPs) across the channel measuring currents in the upper 500 m (Figure 2), the depth range in which the flow is strongest. Moorings on the western side of the channel were also equipped with ADCPs near the bottom, in order to capture the northward flowing Mozambique Undercurrent [*Ridderinkhof and De Ruijter*, 2003]. At intermediate depths and in the deep water on the eastern side of the channel, Recording Current Meters (RCMs) provide point measurements of current velocity at the 1000 m and 1500 m levels. Temperature-salinity-pressure (TSP) sensors were also distributed along the mooring lines at intermediate depths, but since we do not use the TSP sensor data in this study they are not included in Figure 2. One mooring (5a) did not have an upward looking ADCP on top, but instead included three TSP sensors in the upper layer, measuring temperature and salinity at the nominal depths 100, 200 and 400 m. This time series of upper layer hydrographic data from the central part of the channel provides information about the temporal hydrographic variability both representing the whole section [*Van der Werf et al.*, 2009] and in particular the nearby sediment trap mooring. The current meters (RCMs and ADCPs) were set to tide resolving sampling rates of 20 and 30 minutes.

[10] Table 1 shows the data coverage at the different depth levels at each mooring, along with mean and standard deviation of zonal and meridional current components at each instrument or at selected depth levels for the ADCPs. The data return from the moorings was overall high, but some data loss occurred. The upper ADCP at mooring lmc4 (Figure 2) failed during the first deployment period (LOCO I),

and gaps of more than 8 months occurred in the records from two current meters at mooring lmc5a during the third period (LOCO III). Mooring lmc6 could not be recovered at the end of the second deployment, and data from this site are therefore missing for the entire second period (LOCO II). Data return from the last deployment period was highest. Compared to the designed array, only the top ADCP of mooring lmc6 was lacking and replaced by a single point current meter. Time series from 25 observation points are used in this study, of which 14 locations are covered by ADCP and/or RCM for the entire 4.2 years of measurements, while others have coverage for periods ranging between 2.3 and 3.0 years.

[11] Small differences in the actual depths of instruments occurred after mooring redeployments. Improved mooring design reduced mooring knockdown compared to the pilot project, with vertical excursions at the level of the upper ADCPs and RCMs of between 15 and 90 m, while at the deeper instruments the vertical motion was on the order of 5–10 m. In transport calculations the measured depth time series were used to correct for vertical motion.

2.2. Data Treatment

[12] All current velocity records were low pass filtered (forward and backward) with a 3.5 day Butterworth filter and subsampled at daily intervals, to remove tidal and inertial variability. In order to guide spatial interpolation, correlations between current observations at a mooring and between different moorings were determined (Tables 2 and 3). The number of independent observations for the computation of correlations were determined based on the autocorrelation within the various time series, mostly giving joint effective sample sizes of about 50 days. Vertical correlations between the time series at each mooring were strong, at least down to ~1000 m or between levels below 1500 m. Horizontal cor-

Table 1. Mooring Locations and Instrument Types and Depths for the LOCO Mooring Array in the Mozambique Channel[a]

Longitude, Latitude, Depth	Instrument	z	Δz	LOCO I Δt	$\langle u \rangle$	$\sigma(u)$	$\langle v \rangle$	$\sigma(v)$	LOCO II Δt	$\langle u \rangle$	$\sigma(u)$	$\langle v \rangle$	$\sigma(v)$	LOCO III Δt	$\langle u \rangle$	$\sigma(u)$	$\langle v \rangle$	$\sigma(v)$
lmc4 16°32.28S, 40°8.78E, 1351	ADCP	591	100–200	failed					383	−13.4	24.0	−14.2	27.8	664	−22.3	28.5	−24.8	34.1
			200–300							−10.4	16.2	−10.6	18.2		−18.3	18.9	−19.6	21.7
			300–400							−9.8	14.1	−9.8	15.6		−16.8	16.2	−18.2	18.5
			400–500							−9.6	13.4	−9.9	14.5		−16.0	14.6	−17.5	16.9
	ADCP	1340	800–900						379	−7.0	11.4	−6.8	11.4	664	−8.5	9.1	−8.7	10.3
			900–1000							−6.1	11.3	−6.0	11.0		−7.3	9.3	−7.5	10.6
			1000–1100							−4.7	10.6	−4.8	10.4		−5.8	8.6	−5.8	9.8
			1100–1200							−3.3	9.4	−3.3	9.9		−4.0	7.5	−4.1	8.7
	RCM-11(1)	1292	1200–1300	465.5	−0.4	9.7	0.0	12.5		−1.5	7.3	−1.7	8.5		−1.8	5.5	−1.9	7.2
lmc5 16°38.86S, 40°36.82E, 1992	ADCP	591	100–200	468	−24.9	26.3	−27.4	34.6	336.5	−18.5	29.5	−23.3	31.9	664	−24.7	28.7	−33.8	37.4
			200–300		−15.5	16.2	−15.8	22.7		−11.1	19.3	−14.9	19.6		−16.9	18.8	−21.0	24.1
			300–400		−11.6	13.4	−11.7	18.4		−7.9	16.5	−12.0	16.6		−13.0	15.9	−15.7	20.1
			400–500		−10.2	12.8	−10.0	16.5		−6.0	15.0	−10.9	15.2		−11.6	15.2	−13.6	18.2
	RCM[b]	991		468	−4.7	10.9	−5.4	13.0	failed					665	−3.2	8.5	−5.8	10.2
	RCM-11	1491		468	1.3	7.4	1.3	11.9	383.5	1.2	3.6	0.7	6.2	665	−0.2	4.8	−0.9	7.4
	ADCP	1995	1400–1500	468	0.9	5.0	0.4	8.1	383.5	1.7	4.4	1.0	7.0	664	−0.4	5.7	−1.2	8.5
			1500–1600		1.6	5.0	1.4	8.7		1.9	4.3	1.9	7.1		−0.1	5.4	−0.4	8.5
			1600–1700		2.1	4.8	2.3	9.1		2.2	4.3	2.7	7.3		0.3	5.0	0.4	8.8
			1700–1800		2.3	4.5	2.8	9.5		2.2	4.0	3.3	6.9		0.7	4.6	1.3	8.8
			1800–1900		2.3	4.5	3.2	9.5							1.3	3.9	2.5	7.4
lmc5a 16°45.64S, 41°3.76E, 2402	RCM[b]	481		468	−7.6	23.5	−2.3	26.0	383	−1.9	11.5	−1.8	7.6	409	−4.2	15.4	−4.5	15.3
	RCM-11	992		470	−2.1	12.9	0.3	13.7	383	0.0	8.1	−3.2	7.5	114	2.5	5.7	−0.9	5.3
	RCM-11	1491		470	0.8	8.5	1.0	8.5	383	1.6	5.0	−0.9	4.7	665.5	0.2	5.5	0.3	5.9
	ADCP	2391	1800–1900	470	0.9	3.2	1.8	3.9	383	1.9	4.4	1.7	5.2	665.5	0.6	2.9	0.2	3.3
			1900–2000		1.5	3.8	2.6	4.6		2.3	5.1	2.8	6.1		0.2	4.4	0.6	4.8
			2000–2100		2.3	3.8	3.3	4.8		2.7	5.2	3.5	6.2		0.5	5.3	1.2	6.0
			2100–2200		2.4	3.2	3.7	4.7		2.8	4.4	3.9	6.0		1.0	5.6	1.8	6.2
			2200–2300												1.3	4.5	2.5	5.4
lmc6 16°52.26S, 41°28.72E, 2691	ADCP(1)	591	100–200	472	−7.6	34.8	−2.4	35.5						665	−2.6	15.5	1.3	14.9
			200–300		−5.3	25.1	0.5	21.1							−1.3	8.2	−0.1	8.8
			300–400		−3.9	20.2	0.6	16.3							−1.3	5.1	−2.2	6.4
			400–500		−3.7	17.7	0.4	14.3							0.0	3.4	−1.3	5.0
	RCM-11(3)	991		472	−2.2	12.8	−2.0	13.5						665	−0.4	3.0	−2.1	5.3
	RCM-11	1491		471	−2.4	6.7	−4.4	10.6						665	−0.3	4.2	−2.6	7.6
	ADCP	2689	2100–2200	472										664				
			2200–2300															
			2300–2400															
			2400–2500															
			2500–2600												0.1	4.5	−2.2	8.0
			2625–2675		0.1	1.7	−0.3	2.0							0.5	3.6	−1.2	6.5

Table 1. (continued)

Longitude, Latitude, Depth	Instrument	z	Δz	LOCO I					LOCO II					LOCO III				
				Δt	$\langle u \rangle$	$\sigma(u)$	$\langle v \rangle$	$\sigma(v)$	Δt	$\langle u \rangle$	$\sigma(u)$	$\langle v \rangle$	$\sigma(v)$	Δt	$\langle u \rangle$	$\sigma(u)$	$\langle v \rangle$	$\sigma(v)$
lmc7 17°6.24S, 42°56.42E, 1995	RCM-11(1)	621	100–200	478	−0.7	18.4	5.4	18.1	380	15.4	33.3	5.6	30.6	666.5	9.6	39.8	7.9	29.9
	ADCP(2,3)		200–300							7.0	19.4	5.6	19.2		4.4	23.6	6.3	19.2
			300–400							3.6	15.2	5.4	15.3		2.6	16.7	5.8	14.6
			400–500							2.3	14.5	5.4	14.8		1.5	14.9	5.2	13.6
	RCM-11	992		478	1.2	10.7	1.8	9.4	379.5	1.2	6.9	1.8	6.8	666.5	0.7	6.8	1.1	7.0
	RCM-11	1491		478	1.4	7.4	−1.0	7.1	380	−0.4	3.7	−0.2	4.5	666.5	0.0	3.9	−0.3	4.2
lmc8 17°6.24S, 42°28.7E, 2199	ADCP	596	100–200	478	2.7	23.8	7.1	32.6	381.5	16.5	27.2	4.0	30.4	666.5	8.8	30.9	8.4	28.8
			200–300		1.5	13.5	5.0	19.0		7.6	14.5	4.6	18.3		3.6	17.4	5.9	18.2
			300–400		0.9	9.5	4.0	13.9		4.7	9.8	4.1	14.0		1.9	11.4	3.7	12.9
			400–500		0.3	8.2	3.3	12.2		3.7	9.0	3.4	13.2		1.0	10.1	2.7	11.8
	RCM-11	994		478	0.2	5.6	4.4	9.4	381.5	1.0	3.6	2.3	6.0	666.5	−0.1	3.4	1.5	4.6
	RCM[c]	1493		478	−0.4	2.5	−0.8	3.7	381.5	0.2	3.0	0.4	4.7	666.5	0.2	2.0	−0.2	2.9
	RCM[c]	2092		478	0.1	1.6	−1.2	3.1	381.5	0.5	1.7	−1.2	2.6	666.5	0.2	1.5	−1.2	3.0
lmc9 17°14.86S, 43°2.28E, 1439	RCM-11(1,2)	628	100–200	477.5	0.8	4.3	−0.4	14.8						664	4.7	16.0	0.3	35.7
	ADCP(3)		200–300												1.6	7.3	−0.2	21.1
			300–400												0.7	4.9	−0.4	14.8
			400–500												0.3	4.3	−0.5	12.8
			500–600												0.0	3.8	−0.4	11.6
	RCM-11	1026		477.5	−0.1	1.5	1.9	9.8	382	0.2	2.7	3.5	9.9	666	−0.2	1.2	1.4	6.4
	RCM-11(3)	1326							382	−0.2	0.3	4.0	7.0	666	0.1	0.8	−1.6	2.5
lmctrap 16°42.40S, 40°51.06E, 2241	RCM-11(2,3)	1950							382.5	2.4	4.4	2.5	6.0	666.5	0.9	4.7	1.1	7.6
	RCM-11(2,3)	2150							383.5	1.9	4.4	3.6	6.4	176	0.8	4.6	1.6	7.7

[a] Here z is the design depth and Δz is the depth range (m). For the positions of the moorings, see also Figure 2. Record lengths (effective data return, Δt (days), mean ($\langle \ldots \rangle$) and standard deviation (σ) of the eastward (u) and northward (v) velocities are also given (cm/s). ADCP, Acoustic Doppler Current Profiler (RDI LongRanger, 75 kHz); RCM, Recording Current Meters (Aanderaa).

[b] RCM-11 in LOCO-I and RCM-9 in LOCO-II and -III.

[c] RCM-8 in LOCO-I and RCM-11 in LOCO-II and -III.

Table 2. Linear Correlations Between Time Series of Zonal or Meridional Velocity Component at Different Depth Levels at Mooring lmc5 and Correlations Between Zonal, Meridional Velocity Components at the 500 m and 1500 m Depth Levels at Different Moorings[a]

Vertical Within lmc5 (u)

	100 m	500 m	950 m	1500 m	1900 m
100 m	1.00				
500 m	**0.65**	1.00			
950 m	**0.41**	**0.71**	1.00		
1500 m	**0.35**	**0.48**	**0.65**	1.00	
1900 m	**0.27**	0.28	0.30	**0.60**	1.00

Vertical Within lmc5 (v)

	100 m	500 m	950 m	1500 m	1900 m
100 m	1.00				
500 m	**0.70**	1.00			
950 m	**0.49**	**0.75**	1.00		
1500 m	0.28	**0.40**	**0.62**	1.00	
1900 m	0.19	0.24	0.34	**0.71**	1.00

Horizontal, 500 m Level (u)

	lmc4	lmc5	lmc5a	lmc6	lmc7	lmc8	lmc9
lmc4	1.00						
lmc5	**0.49**	1.00					
lmc5a	0.31	**0.76**	1.00				
lmc6	0.23	**0.42**	**0.69**	1.00			
lmc7	0.34	0.17	0.31	**0.61**	1.00		
lmc8	0.28	0.02	0.10	0.26	**0.67**	1.00	
lmc9	0.19	−0.03	−0.02	0.09	0.33	**0.53**	1.00

Horizontal, 1500 m Level (u)

	lmc4	lmc5	lmc5a	lmc6	lmc7	lmc8	lmc9
lmc4	1.00						
lmc5	0.24	1.00					
lmc5a	0.08	0.26	1.00				
lmc6	−0.05	0.03	**0.55**	1.00			
lmc7	0.08	0.28	0.29	**0.38**	1.00		
lmc8	0.03	0.11	−0.19	−0.05	0.26	1.00	
lmc9	0.02	−0.06	−0.03	−0.11	−0.10	−0.06	1.00

Horizontal, 500 m Level (v)

	lmc4	lmc5	lmc5a	lmc6	lmc7	lmc8	lmc9
lmc4	1.00						
lmc5	0.07	1.00					
lmc5a	**−0.43**	**0.47**	1.00				
lmc6	**−0.55**	**−0.48**	0.03	1.00			
lmc7	−0.27	**−0.62**	**−0.32**	**0.62**	1.00		
lmc8	0.01	**−0.50**	**−0.49**	0.13	**0.39**	1.00	
lmc9	0.31	−0.29	−0.36	−0.30	−0.10	0.32	1.00

Horizontal, 1500 m Level (v)

	lmc4	lmc5	lmc5a	lmc6	lmc7	lmc8	lmc9
lmc4	1.00						
lmc5	0.02	1.00					
lmc5a	−0.13	0.00	1.00				
lmc6	−0.21	−0.31	−0.01	1.00			
lmc7	−0.01	−0.12	−0.17	0.21	1.00		
lmc8	0.17	−0.17	−0.08	−0.23	0.04	1.00	
lmc9	0.04	0.04	−0.02	−0.09	0.19	0.03	1.00

[a]Here zonal is u and meridional is v. For the zonal and meridional velocity components of other moorings, see Table 3. Bold values mark correlation coefficients that are statistically significant at the 95% confidence level.

relations between adjacent moorings were mostly moderate to strong at least in the upper 1000 m (Table 2; the level of statistical significance of the correlations is reduced by the strong autocorrelation within each time series). For the zonal component, horizontal correlations were consistently positive, but the meridional components were often negatively correlated between moorings further separated (on each side of the channel). Since velocities at the same mooring were generally strongly (moderately) positively correlated over vertical separations of at least 500 m (1000 m), while the pattern of horizontal correlations was more complicated, inter- or extrapolation of data was done primarily in the vertical.

[13] ADCP data, originally in 8 m depth bins, were vertically averaged to 25 m bins at standard depth levels, which removed the effect of mooring motion. Daily velocities from all instruments on each mooring were linearly interpolated in the vertical onto a 25 m grid. Velocities from the upper 50–100 m, missing due to the loss of near-surface data typical for upward-looking ADCPs, were filled in by linear extrapolation to the surface using the vertical shear from the uppermost four depth levels at each time step. Below the deepest record on each mooring, velocities were linearly extrapolated to 0 at the bottom, except in two cases (mooring lmc7 and lmc9) where the distance from the deepest instrument to the seabed was >400 m. At mooring lmc7, data in the bottom 500 m were filled in by horizontal interpolation between surrounding moorings. At mooring lmc9, measurements from within 100 m of the seabed exist from the last period but not from the two earlier ones. The mean vertical velocity gradient between the 1000 and 1350 m levels during the last period was applied to the data at the 1000 m level from the two earlier deployments in order to extrapolate velocities to the bottom.

[14] Linear interpolation was applied horizontally for each 25 m depth level, to a 1 km horizontal resolution. To fill in the velocity grid between the eastern- and westernmost moorings and the sides of the channel, two methods were tried: (1) extrapolating to zero velocity at the boundary (no slip), and (2) keeping velocity constant from the outermost mooring (full slip). The effects of the different extrapolation methods on the resulting volume transport estimate will be discussed later. The gaps in the transport time series introduced by mooring service and redeployment were filled by linear interpolation in time.

[15] Significant data gaps, namely the upper part of mooring lmc4 during the first deployment, the whole mooring lmc6 during the second, and parts of the records from the current meters at the 500 and 1000 m levels at mooring lmc5a in the last period, were filled with estimates made by multiple linear regression (both horizontal and vertical), based on the time periods with existing data. The regression model for mooring lmc6 used velocity records from surrounding moorings as predictors, in the form

$$V_6(z_{1:N}) = b_0 + b_1 * V_{5a}(z_{1:N}) + b_2 * V_7(z_{1:N}), \qquad (1)$$

where V_6 is the velocity at mooring site 6, V_{5a} and V_7 the velocities at moorings 5a and 7 respectively, $z_{1:N}$ are the depth levels for which velocity will be estimated, and $b_{0,1..}$ are the parameters determined through linear regression.

Table 3. Linear Correlations Between Time Series of Zonal or Meridional Velocity Component at Different Depth Levels at Several Moorings[a]

	Vertical Within lmc4 (u)				Vertical Within lmc4 (v)			
	100 m	500 m	1000 m	1300 m	100 m	500 m	1000 m	1300 m
100 m	**1.00**				**1.00**			
500 m	**0.60**	**1.00**			**0.55**	**1.00**		
1000 m	**0.40**	**0.51**	**1.00**		**0.40**	**0.52**	**1.00**	
1300 m	**0.29**	**0.32**	**0.62**	**1.00**	0.20	0.22	**0.57**	**1.00**

	Vertical Within lmc5a (u)				Vertical Within lmc5a (v)			
	500 m	990 m	1470 m	2000 m	500 m	990 m	1470 m	2000 m
500 m	**1.00**				**1.00**			
990 m	0.54	**1.00**			**0.70**	**1.00**		
1470 m	−0.01	0.47	**1.00**		−0.03	0.14	**1.00**	
2000 m	0.28	0.44	0.40	**1.00**	0.25	0.14	0.41	**1.00**

	Vertical Within lmc6 (u)				Vertical Within lmc6 (v)			
	540 m	960 m	1480 m	2500 m	540 m	960 m	1480 m	2500 m
540 m	**1.00**				**1.00**			
960 m	**0.81**	**1.00**			**0.82**	**1.00**		
1480 m	**0.45**	**0.69**	**1.00**		**0.51**	**0.77**	**1.00**	
2500 m	0.04	0.17	**0.37**	**1.00**	0.17	0.30	**0.60**	**1.00**

	Vertical Within lmc7 (u)				Vertical Within lmc7 (v)			
	100 m	500 m	965 m	1465 m	100 m	500 m	965 m	1465 m
100 m	**1.00**				**1.00**			
500 m	**0.72**	**1.00**			**0.53**	**1.00**		
965 m	**0.51**	**0.76**	**1.00**		0.22	**0.76**	**1.00**	
1465 m	0.32	**0.47**	**0.69**	**1.00**	−0.06	0.28	**0.52**	**1.00**

	Vertical Within lmc8 (u)					Vertical Within lmc8 (v)				
	100 m	500 m	970 m	1465 m	2065 m	100 m	500 m	970 m	1465 m	2065 m
100 m	**1.00**					**1.00**				
500 m	**0.64**	**1.00**				**0.63**	**1.00**			
970 m	**0.39**	**0.65**	**1.00**			**0.41**	**0.70**	**1.00**		
1465 m	0.21	0.19	**0.34**	**1.00**		0.14	**0.30**	**0.56**	**1.00**	
2065 m	−0.01	0.05	0.14	0.16	**1.00**	0.00	0.06	0.14	**0.35**	**1.00**

	Vertical Within lmc9 (u)				Vertical Within lmc9 (v)			
	100 m	500 m	1055 m	1350 m	100 m	500 m	1055 m	1350 m
100 m	**1.00**				**1.00**			
500 m	**0.42**	**1.00**			**0.66**	**1.00**		
1055 m	0.19	**0.22**	**1.00**		0.13	**0.49**	**1.00**	
1350 m	0.05	0.05	0.05	**1.00**	−0.01	0.04	**0.53**	**1.00**

	Vertical Within lmctrap (u)		Vertical Within lmctrap (v)	
	1825 m	2110 m	1825 m	2110 m
1825 m	**1.00**		**1.00**	
2110 m	**0.84**	**1.00**	**0.94**	**1.00**

[a]Bold values mark correlation coefficients that are statistically significant at the 95% confidence level.

[16] For mooring lmc4, LOCO I, a similar model but also using existing data from another depth level (1280 m) on the same mooring was used

$$V_4(z_{1:N}) = b_0 + b_1*V_4(1280) + b_2*V_5(z_{1:N}). \qquad (2)$$

[17] At mooring lmc5a there were by design no velocity measurements above the 500 m level during any deployment period. To fill in the velocity grid for the upper 500 m at this mooring, we chose to use a tapered linear interpolation scheme, whereby the current nearest to the surface is the result of horizontal linear interpolation between the moorings flanking 5a, while each depth bin below this is successively more influenced by the existing data from the 500 m level at 5a, using the following equation:

$$V_{5a}(z) = \frac{(z_c - z)*V_{horiz} + z*V_c}{z_c}, \qquad (3)$$

where z is the depth level for which the velocity V is sought, z_c is the depth of the top current meter at mooring lmc5a, V_c is the velocity measured at this instrument, and V_{horiz} is the
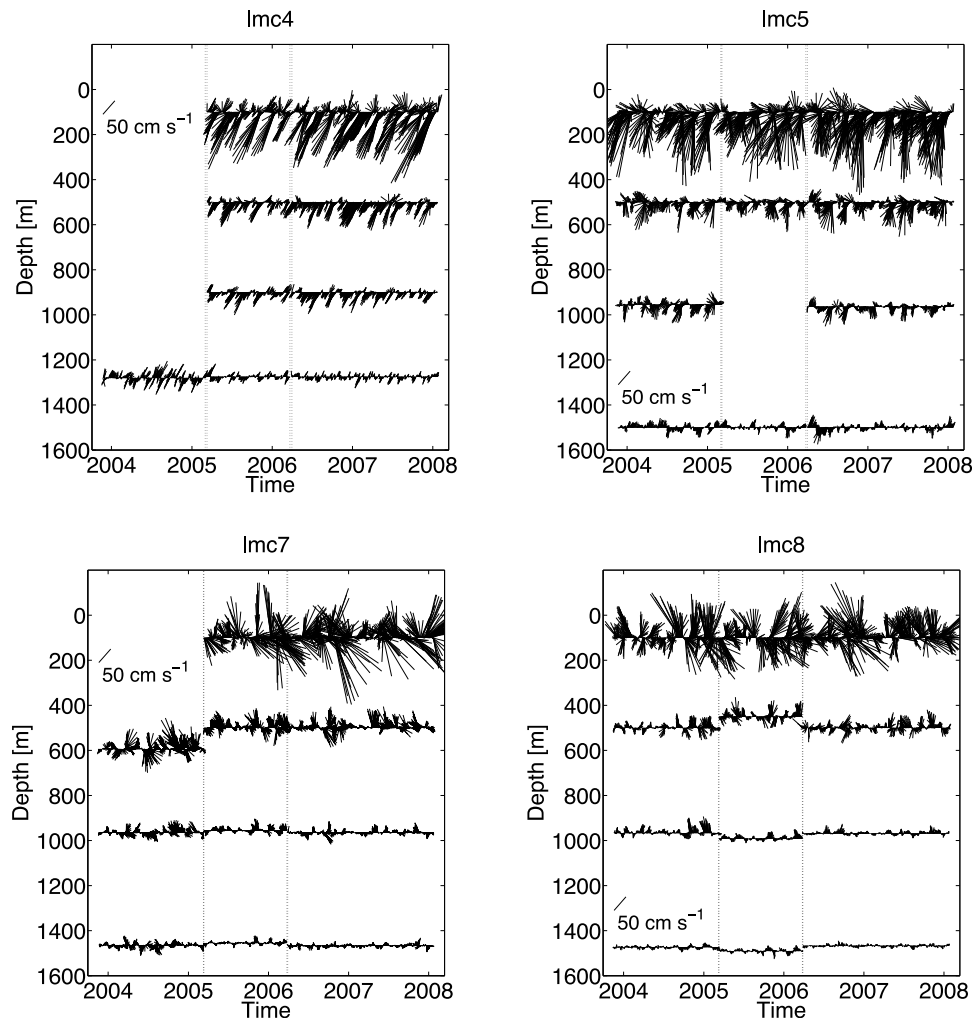
Figure 3. Vector velocity plots of currents at selected depths at moorings (lmc) 4, 5, 7 and 8, with a 50 cm s^{-1} vector plotted for scale. Dotted lines mark deployment breaks.

velocity resulting from horizontal interpolation between the two neighboring moorings.

2.3. Other Data Sources

[18] Apart from the LOCO measurements, this study makes use of a couple of other data sources, to which the transport time series is compared.

[19] The time series of the Indian Ocean Dipole (IOD) index was obtained from http://ioc3.unesco.org/oopc/state_of_the_ocean/. This index [*Saji et al.*, 1999; *Webster et al.*, 1999] is a measure of the zonal gradient of the sea surface temperature anomaly in the tropical Indian Ocean. The index is positive (negative) when the sea surface temperature anomaly of the western tropical Indian Ocean is higher (lower) than that of the eastern tropical Indian Ocean.

[20] The sea surface height anomalies (SSHA) fields were produced by Ssalto/Duacs and distributed by Aviso, with support from CNES. The data was downloaded from http://www.aviso.oceanobs.com/en/data/products/sea-surface-height-products/global/msla/index.html. We used near-real-time data that was gridded on a 1/3° × 1/3° Mercator grid. Geostrophic flow derived from the gradient in sea level

anomaly on the section 10°–15°S, 80°E served as a measure of the strength of the SEC.

[21] Wind fields were obtained from QuikSCAT Level 3 data (http://podaac.jpl.nasa.gov/DATA_PRODUCT/OVW/index.html\#quikscat, product 109), which is daily data gridded on a 0.25° × 0.25° grid. Wind stresses were calculated from this data set, using an approximation for the drag coefficient C_d as proposed by *Smith* [1980]

$$C_d = \frac{1}{1000}(0.61 + 0.063U_{10}), \qquad (4)$$

where U_{10} denotes the wind velocities at 10 m above sea level. From these wind stresses, we computed the wind-driven transport around Madagascar by applying the linear island rule [*Godfrey*, 1989].

3. Observed Velocities at the Mooring Section

[22] Daily current vectors (Figure 3) demonstrate the different character of the currents at the western end compared to the rest of the section, with a stronger preference towards the south–southwest direction. Over most of the
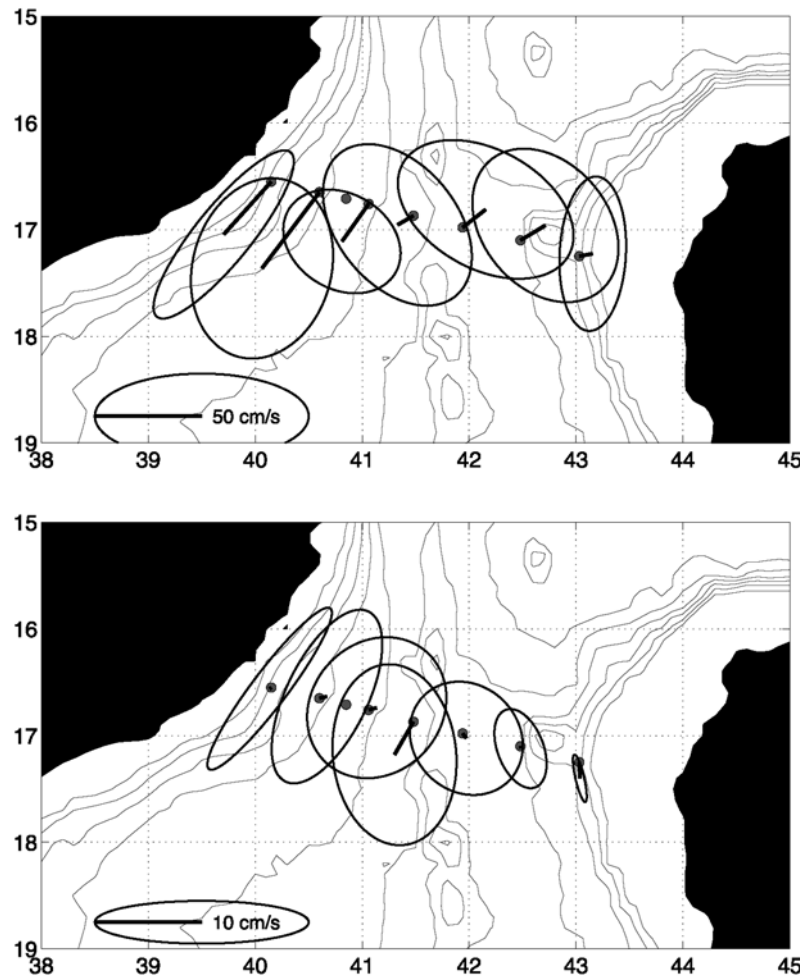
Figure 4. Plan view of the mooring locations with mean velocity vectors at (top) 100 m depth and (bottom) 1500 m depth, with 1 standard deviation ellipses. Mean and standard deviation were computed for the daily, detided data from the whole 4.2 years of measurements.

section the current records down to at least the 1000 m level are dominated by recurring events of strong, rotational motion, representing the passage of anticyclonic eddies that are a well known feature of the circulation in the MC [*Biastoch and Krauss*, 1999; *Ridderinkhof and De Ruijter*, 2003; *Harlander et al.*, 2009].

[23] Mean current vectors and standard deviation ellipses at the 100 and 1500 m (or as near 1500 m as possible) levels for the entire 4.2 years of deployment are shown in Figure 4. Standard deviation of daily, detided current velocity was everywhere relatively high compared to the mean. The strongest mean current at the 100 m depth level was directed towards the southwest and found at the two westernmost moorings. The maximum resultant flow at the western side of the channel was a result not only of high current velocities, but also of the significantly higher level of directional stability of the currents at these locations. The westernmost mooring (mooring lmc4, Figure 3), in 1350 m water depth, showed the highest steadiness or directional persistence of all the moorings, with Neumann factor (the ratio of vector mean to scalar mean, expressed as a percentage, where 100% means unidirectional flow) values for the daily, detided time series of above 70% throughout the upper 900 m.

Here, as well as at the easternmost mooring (lmc9), the standard deviation ellipse was elongated and largely aligned with topography (Figure 4), whereas in the center of the channel, a smaller proportion of the variance is along the major axis. The second mooring from the west (lmc5) also
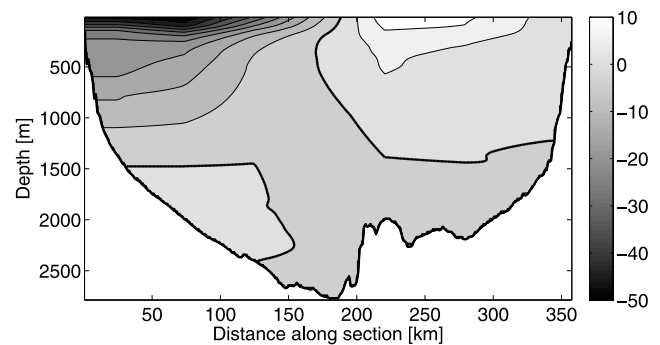
Figure 5. Cross section of mean velocity perpendicular to the mooring section. Velocity is positive northward, with contours at 5 cm s^{-1} intervals; bold line is the zero velocity contour.
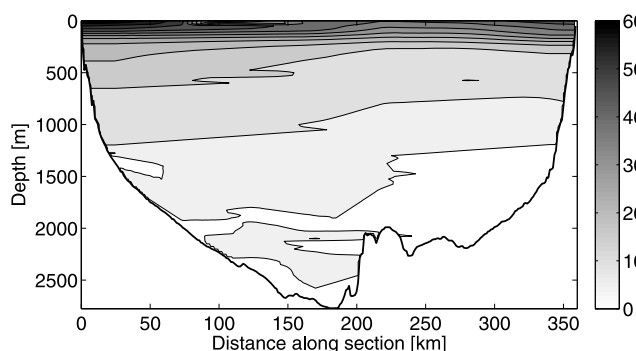
Figure 6. Cross section of standard deviation of velocity perpendicular to the mooring section. White field is the standard deviations ≤5 cm s^{-1}; contours at 5 cm s^{-1} intervals.

had a relatively high level of directional persistence, and in addition the highest current speeds in the upper layers (Figure 3).

[24] The mean velocity cross section also demonstrates the strong southward flow on the western side of the channel (Figure 5). The core of the southward flow was located in the upper 100 m, where the long-term average velocity exceeded 40 cm s^{-1}. The mean current magnitude in the upper layer was similar between the moorings lmc4 and lmc5 (slightly stronger at lmc5), while at levels below the upper few 100 m the poleward flow was strongest and extended the deepest at the westernmost mooring, situated 30 km from the coast in a water depth of 1350 m. Poleward mean velocities extended throughout the upper kilometer of the water column at the two western moorings, weakening with depth to the zero velocity contour which was found at 1500 m at the second mooring from the west in 1990 m water depth.

[25] On the eastern side of the channel, currents were on average equatorward in the upper 1500 m. The northward flow was weaker than the southward flow on the western side, with maximum velocities in the upper 100 m of >10 cm s^{-1}. However, the northward counter flow took up a substantial part of the cross sectional area, covering half of the channel from the center to the eastern edge, and with velocities only reaching zero at about 1500 m depth, like on the western side. The observed mean flow pattern with its east–west asymmetry is most likely the result of the anticyclonic eddies superposed on a background southward flow, but may also be caused or enhanced by eddy self propagation by interaction with the African coast [*Harlander et al.*, 2009].

[26] Leaning on the continental slope on the western side of the channel was the northward flowing deep Mozambique Undercurrent, with mean velocities of 0.3–4.8 cm s^{-1} (varying with depth level and measurement period) and maximum equatorward velocities of up to 35 cm s^{-1}. The strength of the flow in the Undercurrent increased with depth, and thus the highest long-term mean velocities (3.8 cm s^{-1} towards the north–east, averaged over all three deployment periods) were found at the deepest measurement points, in the depth range 2200–2300 m. *Ridderinkhof and De Ruijter* [2003] suggested that the Undercurrent found in the MC might be a continuation of the Agulhas Undercurrent [*Beal and Bryden*, 1997]. The mean velocity of the undercurrent in our measurements was weaker than the 10 cm s^{-1}

observed by *Beal and Bryden* [1997] at 32°S. There are insufficient data from the region between the Agulhas region and the MC to conclude whether there is a continuous current linking the two regions, but model results from a recent study indicate that the link between the Agulhas and Mozambique Undercurrents is weak and the path of the deep water in the region complex, with a large part of the flow being detrained into eddies or into the Agulhas Current, and only a small portion continuing northward along the African continental shelf [*Biastoch et al.*, 2009].

[27] The mean flow structure was qualitatively similar between the different deployment periods, but the strength of the flow varied. The changes in current magnitude occurred on both sides of the 'eddy' part of the flow pattern, i.e. both in the southward flow in the upper western part of the channel, and the northward flow on the eastern side. During the first measurement period, near-surface southward velocities of over 50 cm s^{-1} were found at the western side of the channel, and the northward near-surface velocities on the eastern side exceeded 10 cm s^{-1} between moorings lmc7 and lmc8. While the zero velocity line was found at a similar depth and with similar extension during the second period, the upper layer flows were significantly weaker, with a southward near-surface mean velocity of about 40 cm s^{-1} and northward velocity of <10 cm s^{-1} on the eastern side. During the last deployment period, the eddy velocities were stronger, exceeding 50 cm s^{-1} southward and 15 cm s^{-1} northward. While both northward and southward velocities became stronger, the increase in southward velocities was larger.

[28] Temporal variability of the currents was higher in the western half of the channel, as indicated by the standard deviations of current velocity (Figure 6). Across the channel, current variability was highest in the upper few 100 m of the water column, but at the western end of the section, the 10 cm s^{-1} contour of standard deviation (over the whole 4.2 years) was found well below 1000 m, rather than at 500–700 m depth as on the eastern side. High variability was also found at mooring lmc5a, in particular during the first period, when the velocity standard deviation at 500 m was higher at mooring lmc5a (>20 cm s^{-1}) than anywhere else on the section. At depth, the variability was also higher on the western side and in the deepest part of the channel, contrasting with the deep water on the eastern side of the channel where both mean velocity and standard deviation were close to zero. In short, the distribution of current variability reflects the mean flow in that the strongest mean velocities also have the highest level of variability.

4. Transport

4.1. Volume Transport Calculation

[29] The sensitivity of the volume transport estimate to the interpolation methods and the use of data 'reconstructions' was tested. The choice of horizontal extrapolation method near the channel boundaries makes a difference of about 10% of the total transport. Letting velocities approach zero at the boundary yields a transport that is 1–2 Sv lower (from 0.9 Sv for the weak transport period 2, to 1.9 Sv for period 3) than using constant velocities to the sides. These two approaches could be seen as two extremes (no slip versus
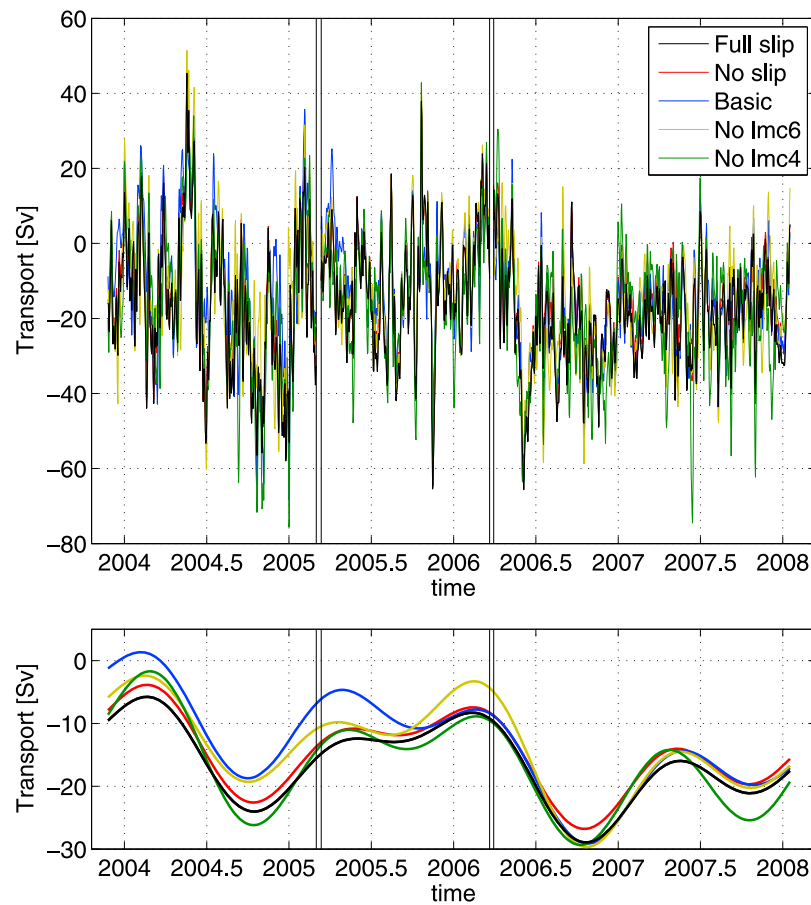
Figure 7. (top) Time series of total volume transport through the section for all three LOCO measurement periods, computed with five different inter- and extrapolation schemes. "No slip" forces 0 velocity at the side boundary, "full slip" keeps velocities constant to the side, "basic" fills large gaps using horizontal interpolation rather than individually adapted gap filling techniques; in "No lmc6" and "No lmc4," data from mooring lmc6 and the upper ADCP in mooring lmc4 is omitted for the whole time series. The vertical lines mark mooring turnovers. (bottom) The same five transport estimates filtered to exclude frequencies higher than 1.2/y.

full slip condition) and the real transport value might be expected to lie between these two endpoints (Figure 7).

[30] As an alternative to the data reconstruction method, transports were also computed using a more basic approach, namely filling all long data gaps by horizontal interpolation. The most complete data set that from the third period was subsampled to correspond to the set with missing data, and new transport estimates for LOCO III were computed. Removing mooring lmc4 (or the upper ADCP at mooring lmc4) made a negligible difference to the total volume transport in the full slip case, but led to a strong underestimation in the no slip case, reducing the mean southward transport by more than 5 Sv. Removing mooring lmc6 led to a less strong but still significant underestimation of the mean transport, of 1.5 Sv. These differences correspond to the transport estimates for the other periods with the basic approach. These tests imply that the filling of large data gaps using the multiple linear regression approach is an improvement over a more basic approach, and reduces the bias otherwise introduced by varying instrument coverage.

[31] The effect of different inter- and extrapolation choices on the time mean transport was our main concern in this study, but it should be noted that the differences in instantaneous (daily) transport values between estimates from different methods are sometimes quite large. The temporal variability of the transport was somewhat higher using our gap-filling method, indicating that the loss of data during some measurement periods leads to an underestimation of the transport variability as well as of the mean transport, unless special care is taken in the filling of these gaps. The mean bias between various methods of approximately 1.5 Sv may serve as an estimate of the systematic error in the transport calculation. Transport values discussed hereafter refer to the time series produced using reconstructed data sets to fill large gaps, and applying the full slip condition for flow near the horizontal boundaries (black line in Figure 7). The resulting mean transport over all three deployment periods amounted to 16.7 Sv poleward, with a standard deviation of 3.1 Sv about the mean.

[32] Maximum northward transport occurred in mid-May 2004. At the peak of northward transport, a strong northward current core was present in the center of the channel, reaching down to 1500 m (Figure 8 (top)). Only a weak southward core, centered at 1000 m depth at mooring lmc5,
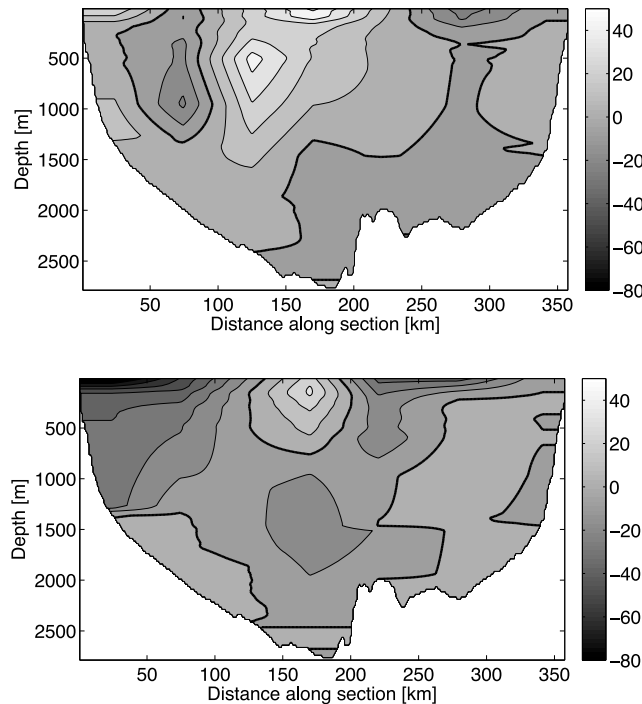
Figure 8. Velocity perpendicular to the mooring section during the maximum northward transport event: (top) 1 week average centered on 17 May 2004 and during the following peak in southward transport and (bottom) 1 week average centered on 28 June 2004. Velocity contours at 10 cm s^{-1} intervals, positive northward; bold line is the zero velocity contour.

was present on the western side of the channel. About 40 days later the transport had shifted to strongly southward, with the more typical strong southward flow at the western side of the channel, strongest at the surface but present almost throughout the whole water column at the western-most site, and surface intensified southward current also found on the eastern side of the channel (Figure 8 (bottom)). Northward transport also peaked in October 2005, when the northward velocities on the eastern side took up more than half of the channel width and the southward flow on the western side was unusually shallow and weak. Maximum southward transport occurred in November 2005. This event was marked by strong and deep-reaching southward flow on the western side of the channel, as well as a relatively strong southward flow in the upper layer on the eastern side.

[33] Our volume transport estimate exceeds that of *Harlander et al.* [2009] based on the same data set for the first two measurement periods, both as regards mean (13.6 Sv for the two first periods compared to their 8.6 Sv) and variability, with daily values ranging from 45 Sv northward to 65 Sv southward rather than 30 and 60 Sv, respectively. The dissimilarity between our transport estimate and that of *Harlander et al.* [2009] is caused by several different choices in terms of methods for filling gaps (temporal and spatial) in the data set. The method changes that contribute the most to the difference in mean transport are the use of a full slip condition at the boundaries, individually adapted gap-filling techniques for large gaps, and the extrapolation

to the surface while the estimate of *Harlander et al.* [2009] only included depths greater than 50 m. The sensitivity analyses of both studies suggest that the loss of mooring lmc6 and partial loss of mooring lmc4 lead to an underestimation of the transport; in this study we have attempted to compensate for these losses by using the data from the last, very successful mooring period as a basis for interpolation. In agreement with the earlier study we find that the changes in transport between different periods, e.g. the significantly lower transport during the second period, are not simply artifacts due to changes in measurement coverage, but are real effects.

[34] Our choice to use, where possible, vertical inter- and extrapolation at each mooring site before horizontal gridding, is based on the observation that vertical correlations between observation points on a mooring in general are considerably higher than horizontal correlations between moorings (section 2.2 and Table 2). Furthermore, we had access to the most complete (LOCO III) data set to date which was used as a reference in our calculations. For these reasons we believe our transport estimate is an improvement on the previous estimate. Either way, the choice of methods does not affect the main features of the transport time series, such as the large transitions both with respect to mean transport and (dominant frequencies of) variability.

[35] The power spectrum of this time series is shown in Figure 9. It shows a clear peak at a frequency of five to six times a year, i.e., a period of around 70 days, which was also observed in previous studies [e.g., *Schouten et al.*, 2003; *Harlander et al.*, 2009; *Van der Werf et al.*, 2010]. At longer time scales, the variability is mainly at frequencies around 1/y (seasonal cycle) and 0.5/y, although neither peak is significant to an AR(1) red noise spectrum. This red noise spectrum was computed with a Monte Carlo simulation with 5000 members. The insignificance is due to the relatively short length of the time series and the strong variability at high frequencies. Nevertheless, in the next section, the origin of
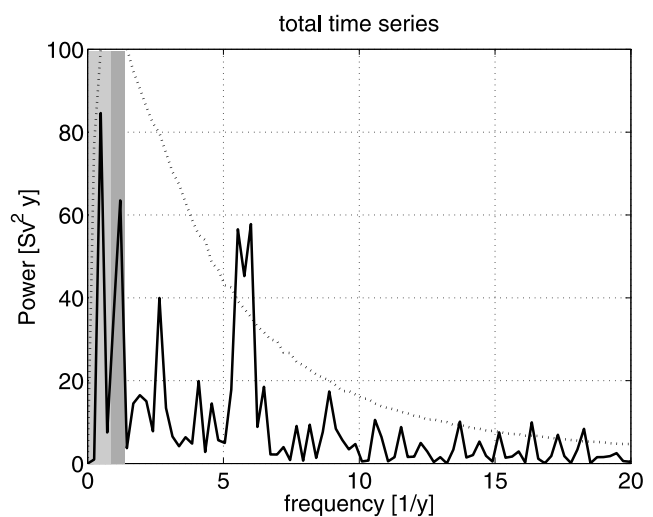

Figure 9. Power spectrum of the transport. The dotted line denotes the 95% confidence interval of an AR(1) red noise spectrum. The two vertical grey bands show the frequency range over which the transport time series was filtered in Figure 10.
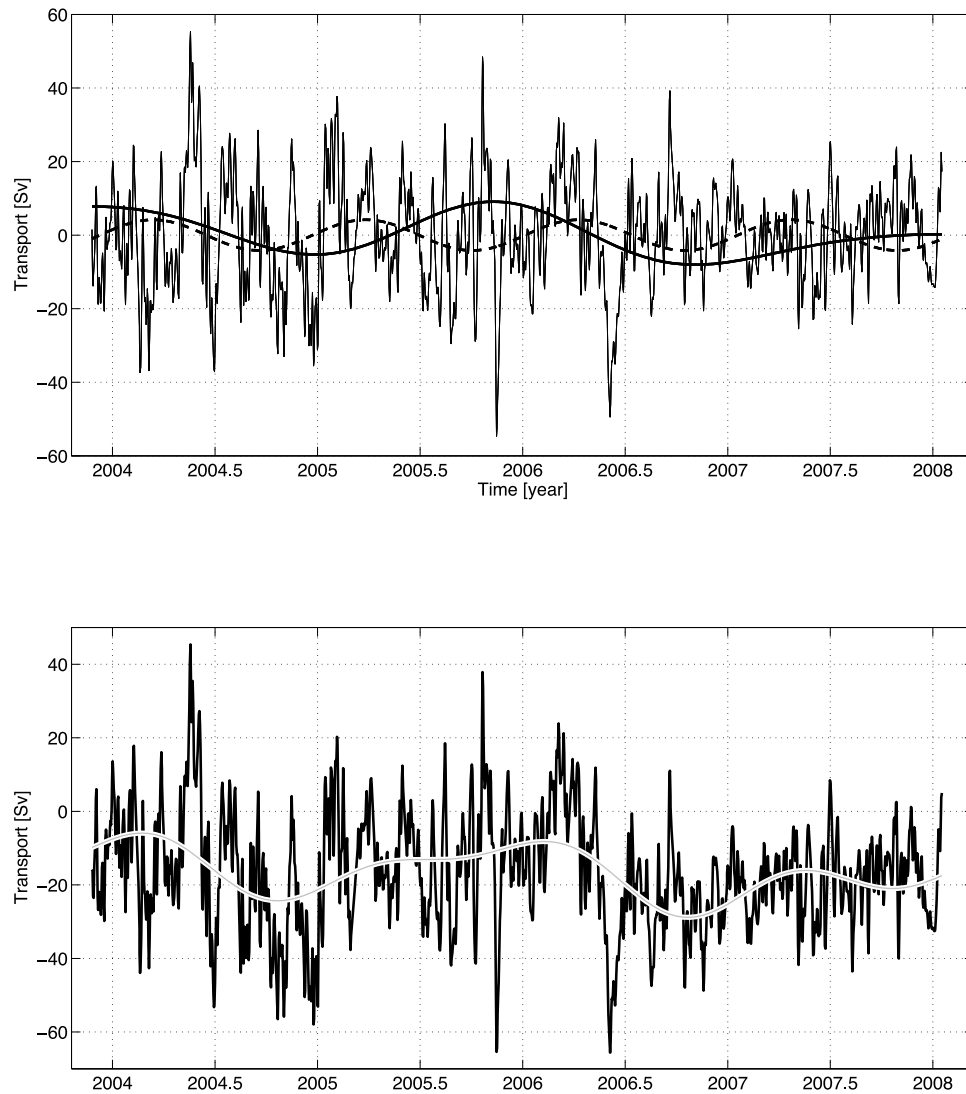
Figure 10. (top) The transport time series decomposed into three frequency bands: the low frequency band (0–0.9/y, thick solid line), the yearly frequency band (0.9/y–1.2/y, thick dashed line), and the high frequency band (1.2/y–100/y, thin solid line). (bottom) The original transport time series (black line) and the superposition of the transport in the low and yearly frequency bands (gray line). The superposition neatly follows the long-term variability of the transport.

the variability at these long time scales will be discussed. Wavelet analysis shows that both the seasonal cycle and the signal with a frequency of 0.5/y are strong throughout the whole time series.

[36] Compared to the frequency spectrum of the first two deployment periods, computed in the study of *Harlander et al.* [2009], the spectrum of the full 4.2 year time series is similar in a qualitative way, as the peaks lie around the same frequencies. However, the variability around five to six times a year is somewhat lower in this study, although still significant. We will not elaborate on this change in this study, but focus mainly on the longer time scales.

4.2. Transport Time Series in Three Frequency Bands

[37] Also by comparing the means of the transport in the three periods, it is apparent that there is variability at longer

time scales. In the first deployment period, the mean transport was 16.0 Sv southward. In the second period, the transport was relatively weak, with a mean of 10.8 Sv southward. The mean transport of the third deployment period was strongest: 20.6 Sv southward.

[38] To examine the variability at longer time scales, the transport time series was decomposed into three frequency bands (Figure 10 (top)), by filtering it in the frequency domain. The selection of frequency bands was based on the power spectrum of the transport (Figure 9). The low frequency band consists of frequencies between zero and 0.9/y. Over the whole time series, the dominant period of the transport in this band is 2 years; its maximum amplitude is 8.9 Sv. The second frequency band is the yearly cycle (frequencies between 0.9/y and 1.2/y). The amplitude of the transport in this band has a maximum of 4.1 Sv. Finally, in
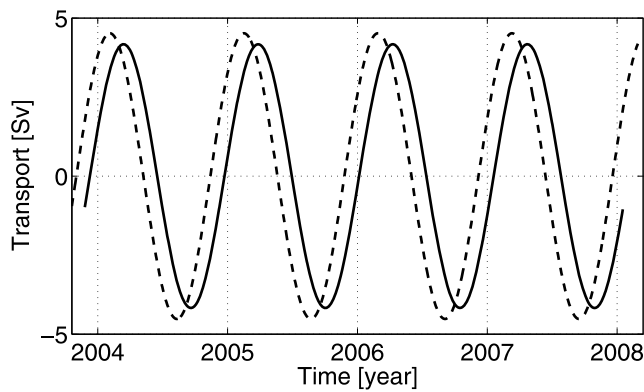
Figure 11. Time series of the band filtered (0.9/y–1.2/y) observed Mozambique Channel transport (solid line) and the calculated transport through the channel induced by the winds west of 75°E (dashed line).

the high frequency band all frequencies higher than 1.2/y are combined. The transport in this band has the largest range of the three bands, and varies between 55.3 Sv northward and 54.6 Sv southward.

[39] The variability at longer time scales is the superposition of the variability in the low frequency band and the yearly frequency band (Figure 10 (bottom)). For example, the transport increase in May 2006 (see Figure 7) was due to an increase in both bands. Before this event, in the austral summer of 2005–2006, the total transport was weak because of the canceling effect of the opposed transports in the low and yearly frequency bands. The total transport increased in May 2006, when the transport in both the low frequency band and the yearly band had the same (southward) direction and increased. Meanwhile, there was a sharp peak in the transport in the high frequency band. This resulted in a very sharp increase in the total transport. Afterwards, the total transport remained strong since especially the transport in the low frequency band remained (strongly) southward. A similar analysis can be given for the decrease of the mean transport in the end of 2004 to the beginning of 2005.

[40] Thus, these interannual transport changes occur because of the almost parallel increase of the transport with a small phase shift in the low and yearly frequency bands. To understand the origin of the variability of the transport at these longer time scales, the causes of the variability in the yearly and low frequency bands are investigated in the next section.

4.3. Origin of the Variability in the Yearly and Low Frequency Band

[41] The transport in the yearly frequency band is primarily related to the wind stress pattern in the Indian Ocean. *Matano et al.* [2002, 2008] showed that regional barotropic processes control the seasonal variability in the south Indian Ocean. The origin of the seasonal variability of the transport in the MC should therefore be found west of 75°E [see *Matano et al.*, 2008, Figure 3a], since the seasonal variability cannot cross the Mid Indian Ridge. The Island Rule [*Godfrey*, 1989] allows the estimation of transport west of an island by applying a Sverdrup model of wind-driven transport to the ocean east of it. In a steady state, the north-

ward transport west of the island, e.g., in the Mozambique Channel, can be expressed as the path integral of wind stress over the ocean between the island and 75°E

$$T_0 = -\frac{1}{\rho_0(f_N - f_S)} \oint_C \tau \cdot dl, \qquad (5)$$

where C is the contour around a domain delimited by the western perimeter of the island, the latitudes of the northern and southern tips of the island, and a meridional boundary at 75°E between the same latitudes; f_N and f_S are the Coriolis parameter on the northern and southern latitude, respectively; τ is the wind stress and dl is a line element of the contour. ρ_0 is the density of the water and taken to be 1030 kg m^{-3}. Using the wind stress computed from the QuikSCAT wind field west of 75°E, the linear island rule yielded a transport variability in the MC of about 4.5 Sv in the frequency band 0.9–1.2/y (Figure 11). This is slightly higher than the amplitude of the transport in the yearly band observed in the channel. The amplitude of both signals varies slightly (about 0.1 Sv) over the length of the time series. The lag between the wind forcing and the transport is about a month, consistent with the propagation speed of the seasonal cycle as shown in Figure 4 of *Matano et al.* [2008].

[42] In the lowest frequency band (<0.9/y) we did not find a significant correlation between the MC transport and wind stress west in the Indian Ocean, although for example *Horii et al.* [2008] have shown that there were anomalous winds in the tropics preceding the positive IOD phase of 2006 [see also *Reason et al.*, 2000]. The low frequency part of the island rule-induced MC transport by the anomalous wind stress [*Godfrey*, 1989] was maximum in April 2006, when it contributed an extra 2.3 Sv to the transport. This was 26% of the maximum southward low frequency transport of 8.9 Sv. Nevertheless, for most of the 4.2 year time series, the wind induced transport in the subannual frequency band was out of phase with the channel throughflow, as it had a different periodicity of 14 months instead of about 2 years.

[43] The transport variability in the lowest frequency band is thus not directly related to variability in the wind field of the Indian Ocean. Instead, it is presumably related to large scale variability in the ocean circulation upstream. It is therefore highly likely that this variability is transported by the SEC, which is the source of water of the Madagascar region (see Figure 1) [*Schott et al.*, 2009]. The strength of the SEC is related to the strengths of the subtropical and tropical gyres and to the strength of the Indonesian Throughflow. In its turn, the strength of the tropical gyre is related to large scale tropical variability, such as the IOD.

[44] In Figure 12, the low frequency variability of the MC transport (equal to the thick solid line in Figure 10 (top)), the zonal velocity anomaly of the SEC and the IOD index are shown. The strength of the SEC is derived from the gradient in sea level anomaly from Aviso at 80°E and at the section 10°–15°S (the meridional lines in Figures 1 and 13), by using the geostrophic balance.

[45] The low pass filtered zonal velocity of the SEC and the low pass filtered transport in the MC are positively correlated. In July 2004 and January 2006, the SEC had a maximum westward flow, of respectively 4.2 cm s^{-1} and 8.1 cm s^{-1}. Assuming a current width of 5° and 200 m
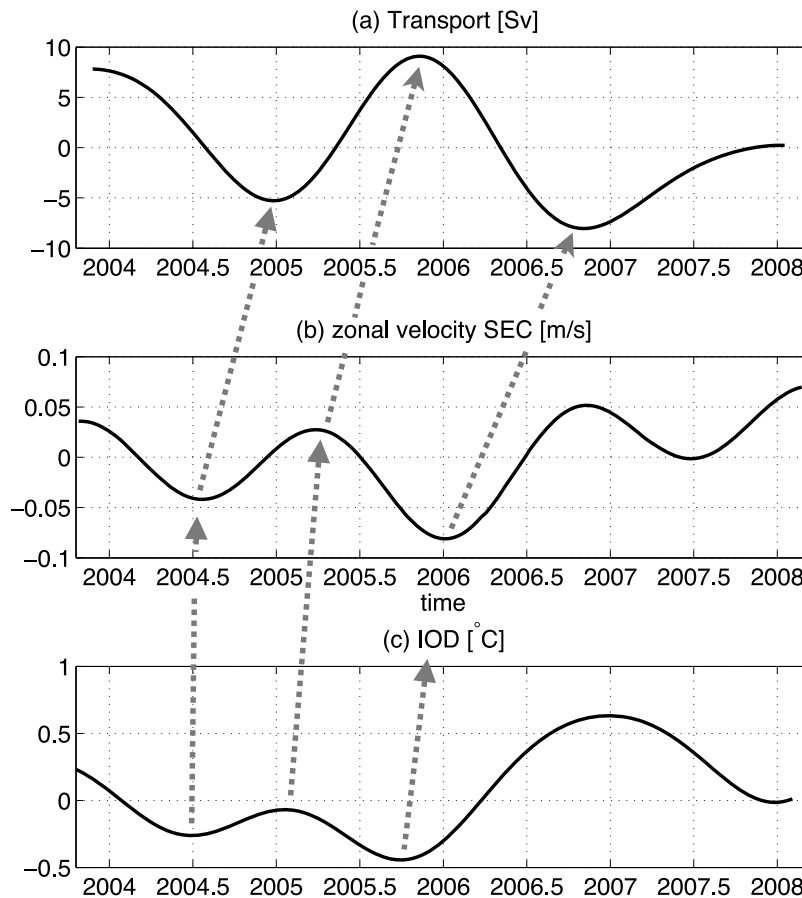
Figure 12. Time series of (a) low frequency variability of the Mozambique Channel transport, (b) zonal velocity anomaly of the SEC, and (c) the IOD index. The zonal velocity of the SEC was derived from a SSHA time series (80°E; 10°–15°S; Figures 1 and 13) by using the geostrophic balance.

depth [*Conkright et al.*, 2002], this is equivalent to a transport anomaly of 4.7 Sv and 8.9 Sv, respectively. A couple of months later, these anomalies were followed by a maximum southward transport through the section with a similar magnitude. After an anomalous eastward flow in the SEC, the southward flow in the MC weakened, for example in the austral summer of 2005–2006. The correlation between transport and SEC strength is significant to an 80% confidence level. This level was based on the 11 individual members of the transport time series which was determined by its autocorrelation function (the SEC time series had 14 individual members). The correlation coefficient is 0.48 where the SEC leads the transport by 8.6 months. This lag can be explained by the speed of a baroclinic wave with a Rossby radius of deformation of 100 km [*Chelton et al.*, 1998, Figure 6] traveling with a speed of 20 cm s^{-1}.

[46] The strength of the SEC anomaly is probably related to the sea level anomaly changes by the IOD cycle and by changes in the Indonesian Throughflow. The low pass filtered IOD index (Figure 12c) has a similar shape as the low pass filtered SEC strength, although the amplitudes of the IOD index are not consistent with the other two time series. Nevertheless, the time series of the IOD index and the SEC anomaly are positively correlated to a confidence level of 90% with a correlation coefficient of 0.60 (the number of

individual members of the IOD index is 11). The lag between the time series is 2.3 months.

[47] In the 1.5 years of the studied period, from January 2004 to July 2005, there were no large gradients of the SSHA in the the tropical Indian Ocean (Figure 13). The anomaly in the strength of the SEC was therefore relatively small. In October 2005 this changed, as the IOD index was in a negative phase. The SSHA gradients in the Indian Ocean became therefore somewhat stronger. A negative anomaly in SSH appeared around 80°E; 8°S (Figure 13, October). This anomaly increased and moved westward (January 2006), just as during the IOD in 1997 [*Webster et al.*, 1999; *Rao et al.*, 2002; *Feng and Meyers*, 2003]. It strengthened the tropical gyre and thereby intensified the SEC. In April 2006, the negative phase of the IOD was ending, as the negative SSH anomaly weakened. While the IOD index transferred to its positive state, the signal induced by the negative state traveled westward.

[48] The strength of the Indonesian Throughflow has a variability over long time scales. The Indonesian Through-flow feeds directly into the SEC [*Gordon*, 1986; *Song et al.*, 2004; *Talley and Sprintall*, 2005]. *Sprintall et al.* [2009] observed a weaker Indonesian Throughflow transport around November 2004 and a stronger transport around
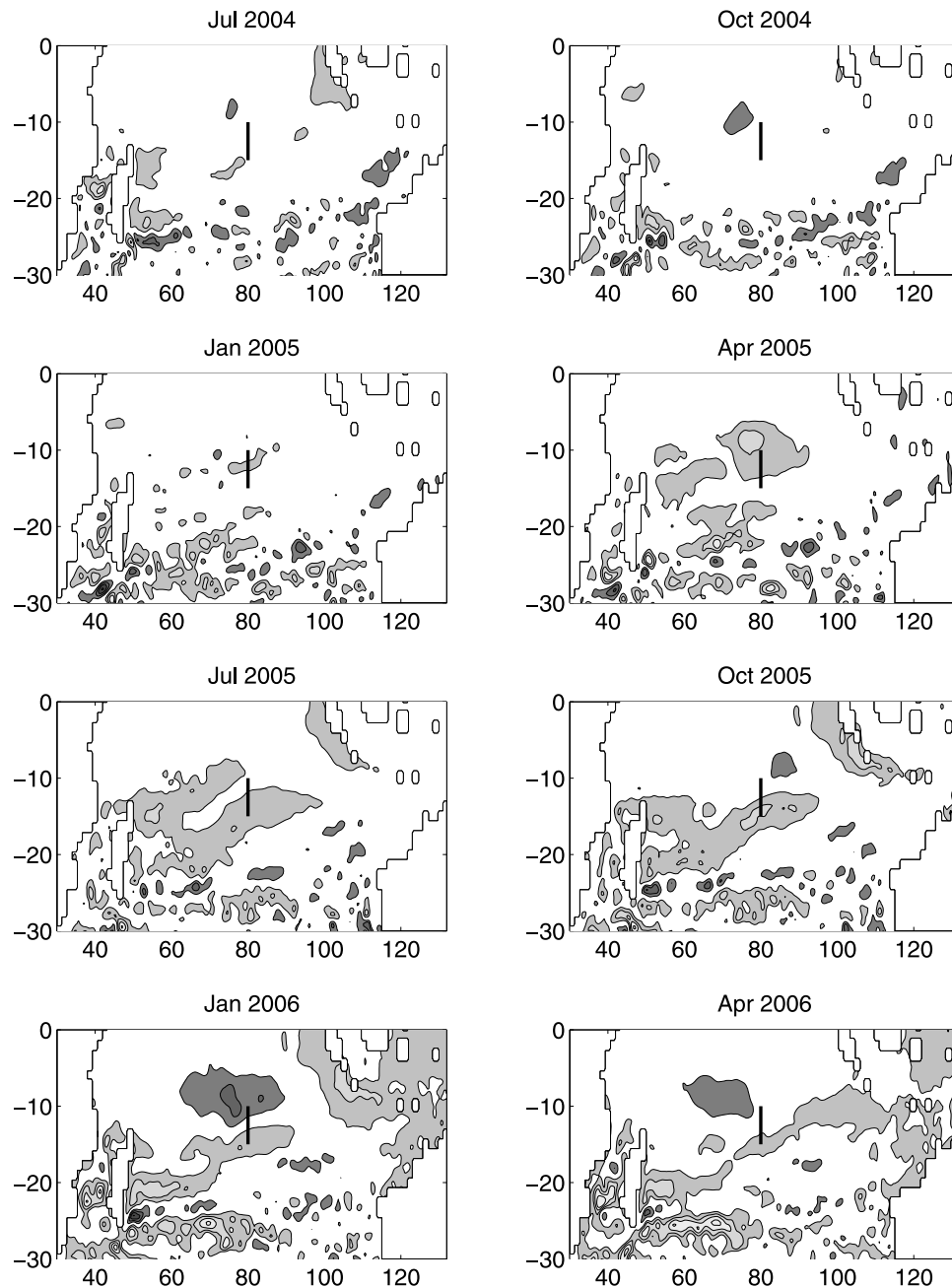
Figure 13. Eight snapshots of low pass filtered SSHA in the Indian Ocean from July 2004 to April 2006. The black line in each denotes the section along which the strength of the SEC was determined. Contours are drawn every 5 cm, darker (lighter) colors are negative (positive) values. The values between −5 cm and 5 cm are omitted.

July–August 2005. This seems to be in agreement with the observed anomalies in the SEC (Figure 12).

5. Discussion and Conclusions

[49] The long-term data set from an array of current meter moorings in the MC offers excellent opportunities to study variability in currents and volume transports in this branch of the large scale circulation of the Indian Ocean. Quantitative estimates on variability in the long-term volume transport are sensitive to the spatial interpolation that is applied to obtain a complete coverage of currents on the entire cross section, especially if spatial gaps are present in the basic data set. Repeated periods of observations are very useful in order to be able to derive interpolation schemes for an estimate of currents at locations where no observations are available.

[50] The mean volume transport through the channel was 16.7 Sv poleward, with a standard error of 3.1 Sv (based on an integral time scale of 30 days). Daily transport values ranged between 45.4 Sv northward and 67.2 Sv southward. The length of the observations, covering more than 4 years,

allows a study on the variability in the volume transport on seasonal and interannual time scales. Seasonal variability has an amplitude of about 4 Sv with the strongest southward currents in the austral winter. The amplitude of this signal is remarkably close to an estimate based on an application of the island rule using the observed seasonal variability in the winds in a region to the west of the Mid Indian Ridge in the southern Indian Ocean.

[51] Variability on interannual time scales in the volume transport in the MC is remarkably large (the variability is of the same order as the mean) and the observed variability in the transport can be related to large-scale physical phenomena. The interannual transport variability seems to be closely related to variability in the Indian Ocean Dipole (IOD) index and, presumably interrelated, variability in the Indonesian throughflow. Satellite observations on anomalies in the sea surface gradient across the SEC suggest that a relatively strong (weak) southward volume transport through the MC is related to an increased (decreased) westward transport in the SEC. The changes in the strength of the SEC lead the changes in the MC volume transport with a lag of about 8–9 months. A similar relationship between the SEC and the MC throughflow has been described by *Palastanga et al.* [2006]. Their Figure 10 shows that in the period 1993 to 2003, a few months after the strengthening (weakening) of the SEC, the strength of the North East Madagascar Current (NEMC) increases (decreases), followed by an increase (decrease) of the strength of the MC throughflow.

[52] There thus seems to be a positive correlation between the IOD cycle and the transport through the Mozambique section: A positive IOD index causes a weakening of the tropical gyre and in the end a weaker southward transport through the channel, while a negative IOD index strengthens the tropical gyre, which is followed by a stronger, southward transport. The coupling via the SEC is essential, as the IOD index itself is not significantly correlated to the Mozambique Channel transport. The lag between the IOD phase and the transport in the MC in the studied time span is roughly 1 year, about half of the typical IOD time scale. Therefore, a positive IOD index coincides with a period of more southward MC transport (Figure 12). This could lead to incorrect interpretations of cause-effect relations. For example, *Palastanga et al.* [2006] observed a southward transport increase just after the positive IOD phase of 1997/1998, and concluded that the positive IOD phase caused the transport increase. However, this is inconsistent with our time series, as we observed a transport increase just before the IOD+ phase of 2006 (Figure 12). Our explanation, i.e., a negative IOD phase causes a transport increase after a lag of about 1 year, explains both the transport increases of 1997/1998 and of May 2006.

References

Beal, L. M., and H. L. Bryden (1997), Observations of an Agulhas Undercurrent, *Deep Sea Res. Part I*, *44*(9–10), 1715–1724.

Biastoch, A., and W. Krauss (1999), The role of mesoscale eddies in the source regions of the Agulhas Current, *J. Phys. Oceanogr.*, *29*, 2303–2317.

Biastoch, A., L. M. Beal, J. R. E. Lutjeharms, and T. G. D. Casal (2009), Variability and coherence of the Agulhas Undercurrent in a high-resolution ocean general circulation model, *J. Phys. Oceanogr.*, *39*, 2417–2435, doi:10.1175/2009JPO4184.1.

Chelton, D. B., R. A. DeSzoeke, M. G. Schlax, K. El Naggar, and N. Siwertz (1998), Geographical variability of the first baroclinic Rossby radius of deformation, *J. Phys. Oceanogr.*, *28*, 433–460.

Conkright, M. E., R. A. Locarnini, H. E. Garcia, T. D. O'Brien, T. P. Boyer, C. Stephens, and J. I. Antonov (2002), World Ocean Atlas 2001: Objective analyses, data statistics and figures [CD-ROM], *Internal Rep. 17*, Natl. Oceanogr. Data Cent., Silver Spring, Md.

Cunningham, S., et al. (2007), Temporal variability of the Atlantic Meridional Overturning Circulation at 26.5°N, *Science*, *317*, 935–937.

De Ruijter, W. P. M., A. Biastoch, S. S. Drijfhout, J. R. E. Lutjeharms, R. P. Matano, T. Pichevin, P. J. Van Leeuwen, and W. Weijer (1999), Indian-Atlantic interocean exchange: Dynamics, estimation and impact, *J. Geophys. Res.*, *104*(C9), 20,885–20,910.

De Ruijter, W. P. M., H. Ridderinkhof, and M. W. Schouten (2005), Variability of the southwest Indian Ocean, *Phil. Trans. R. Soc. London Ser. A*, *363*, 63–76.

DiMarco, S. F., P. Chapman, W. D. Nowlin Jr., P. Hacker, K. Donohue, M. Luther, G. C. Johnson, and J. Toole (2002), Volume transport and property distributions of the Mozambique Channel, *Deep Sea Res. Part II*, *49*(7–8), 1481–1511, doi:10.1016/S0967-0645(01)00159-X.

Feng, M., and G. Meyers (2003), Interannual variability in the tropical Indian Ocean: A two-year time-scale of Indian Ocean Dipole, *Deep Sea Res. Part II*, *50*, 2263–2284, doi:10.1016/S0967-0645(03)00056-0.

Godfrey, J. S. (1989), A Sverdrup model of the depth-integrated flow for the World Ocean allowing for island circulations, *Geophys. Astrophys. Fluid Dyn.*, *45*, 89–112.

Gordon, A. L. (1986), Interocean exchange of thermocline water, *J. Geophys. Res.*, *91*(C4), 5037–5046.

Harlander, U., H. Ridderinkhof, M. W. Schouten, and W. P. M. De Ruijter (2009), Long-term observations of transport, eddies, and Rossby waves in the Mozambique Channel, *J. Geophys. Res.*, *114*, C02003, doi:10.1029/2008JC004846.

Horii, T., H. Hase, I. Ueki, and Y. Masumoto (2008), Oceanic precondition and evolution of the 2006 Indian Ocean dipole, *Geophys. Res. Lett.*, *35*, L03607, doi:10.1029/2007GL032464.

Johns, W. E., T. N. Lee, D. Zhang, R. Zantopp, C. T. Liu, and Y. Yang (2001), The Kuroshio east of Taiwan: Moored transport observations from the WOCE PCM-1 array, *J. Phys. Oceanogr.*, *31*, 1031–1051.

Lutjeharms, J. R. E. (2006), *The Agulhas Current*, Springer, Berlin.

Matano, R. P., E. J. Beier, P. T. Strub, and R. Tokmakian (2002), Large-scale forcing of the Agulhas variability: The seasonal cycle, *J. Phys. Oceanogr.*, *32*, 1228–1241.

Matano, R. P., E. J. Beier, and P. T. Strub (2008), The seasonal variability of the circulation in the South Indian Ocean: Model and observations, *J. Mar. Syst.*, *74*(1–2), 315–328, doi:10.1016/j.jmarsys.2008.01.007.

Nauw, J. J., H. M. Van Aken, A. Webb, J. R. E. Lutjeharms, and W. P. M. De Ruijter (2008), Observations of the southern East Madagascar Current and undercurrent and countercurrent system, *J. Geophys. Res.*, *113*, C08006, doi:10.1029/2007JC004639.

Palastanga, V., P. J. Van Leeuwen, and W. P. M. De Ruijter (2006), A link between low frequency meso-scale eddy variability around Madagascar and the large-scale Indian Ocean variability, *J. Geophys. Res.*, *111*, C09029, doi:10.1029/2005JC003081.

Palastanga, V., P. J. Van Leeuwen, and W. P. M. De Ruijter (2007), Flow structure and variability in the subtropical Indian Ocean: Instability of the South Indian Ocean Countercurrent, *J. Geophys. Res.*, *112*, C01001, doi:10.1029/2005JC003395.

Rao, S. A., S. K. Behera, Y. Masumoto, and T. Yamagata (2002), Interannual subsurface variability in the Tropical Indian Ocean with a special emphasis on the Indian Ocean Dipole, *Deep Sea Res. Part II*, *49*, 1549–1572.

Reason, C. J. C., R. J. Allan, J. A. Lindesay, and T. J. Ansell (2000), ENSO and climatic signals across the Indian Ocean Basin in the global context: Part I, Interannual composite patterns, *Int. J. Climatol.*, *20*(11), 1285–1327, doi:10.1002/1097-0088.

Ridderinkhof, H. (2005), RSS Discovery cruise report: Cruise D289B—Mozambique Channel, 26 February–15 March 2005, technical report, R. Neth. Inst. for Sea Res., Texel, Netherlands.

Ridderinkhof, H. (2008), FS METEOR cruise report: Cruise M75-1B—Mozambique Channel, 19 January–4 February 2008, technical report, R. Neth. Inst. for Sea Res., Texel, Netherlands.

Ridderinkhof, H., and W. P. M. De Ruijter (2003), Moored current observations in the Mozambique Channel, *Deep Sea Res. Part II*, *50*, 1933–1955.

Ridderinkhof, H., and G. D. Quartly (2006), RSS Discovery cruise report: Cruise D301B and D302—Indian Ocean, 20 March–11 April 2006, technical report, R. Neth. Inst. for Sea Res., Texel, Netherlands.

Saji, N. H., B. N. Goswami, P. N. Vinayachandran, and T. Yamagata (1999), A dipole mode in the tropical Indian Ocean, *Nature*, *401*, 360–363.

Schott, F. A., T. N. Lee, and R. Zantopp (1988), Variability of structure and transport of the Florida Current in the period range of days to seasonal, *J. Phys. Oceanogr.*, *18*, 1209–1230.

Schott, F. A., S.-P. Xie, and J. P. McCreary Jr. (2009), Indian Ocean circulation and climate variability, *Rev. Geophys.*, *47*, RG1002, doi:10.1029/2007RG000245.

Schouten, M. W., W. P. M. De Ruijter, P. J. Van Leeuwen, and H. A. Dijkstra (2002), An oceanic teleconnection between the equatorial and southern Indian Ocean, *Geophys. Res. Lett.*, *29*(16), 1812, doi:10.1029/2001GL014542.

Schouten, M. W., W. P. M. De Ruijter, P. J. Van Leeuwen, and H. Ridderinkhof (2003), Eddies and variability in the Mozambique Channel, *Deep Sea Res. Part II*, *50*, 1987–2003.

Sheinbaum, J., J. Candela, A. Badan, and J. Ochoa (2002), Flow structure and transport in the Yucatan Channel, *Geophys. Res. Lett.*, *29*(3), 1040, doi:10.1029/2001GL013990.

Smith, S. D. (1980), Wind stress and heat flux over the ocean in gale force winds, *J. Phys. Oceanogr.*, *10*, 709–726.

Song, Q., A. L. Gordon, and M. Visbeck (2004), Spreading of the Indonesian Throughflow in the Indian Ocean, *J. Phys. Oceanogr.*, *34*, 772–792.

Sprintall, J., S. Wijffels, R. Molcard, and I. Jaya (2009), Direct estimates of the Indonesian Throughflow entering the Indian Ocean, *J. Geophys. Res.*, *114*, C07001, doi:10.1029/2008JC005257.

Stammer, D., C. Wunsch, R. Giering, C. Eckert, P. Heimbach, J. Marotzke, A. Adcroft, C. Hill, and J. Marshall (2003), Volume, heat, and freshwater transports of the global ocean circulation 1993–2000, estimated from a general circulation model constrained by World Ocean Circulation Experiment (WOCE) data, *J. Geophys. Res.*, *108*(C1), 3007, doi:10.1029/2001JC001115.

Talley, L. D., and J. Sprintall (2005), Deep expression of the Indonesian Throughflow: Indonesian Intermediate Water in the South Equatorial Current, *J. Geophys. Res.*, *110*, C10009, doi:10.1029/2004JC002826.

Van Aken, H. M., H. Ridderinkhof, and W. P. M. De Ruijter (2004), North Atlantic deep water in the south–western Indian Ocean, *Deep Sea Res. Part I*, *51*(6), 755–776, doi:10.1016/j.dsr.2004.01.008.

Van der Werf, P. M., M. W. Schouten, P. J. Van Leeuwen, H. Ridderinkhof, and W. P. M. De Ruijter (2009), Observation and origin of an interannual salinity anomaly in the Mozambique Channel, *J. Geophys. Res.*, *114*, C03017, doi:10.1029/2008JC004911.

Van der Werf, P. M., P. J. Van Leeuwen, H. Ridderinkhof, and W. P. M. De Ruijter (2010), Comparison between observations and models of the Mozambique Channel transport: Seasonal cycle and eddy frequencies, *J. Geophys. Res.*, *115*, C02002, doi:10.1029/2009JC005633.

Webster, P. J., A. M. Moore, J. P. Loschnigg, and R. R. Leben (1999), Coupled ocean-atmosphere dynamics in the Indian Ocean during 1997–98, *Nature*, *401*, 356–360.

W. P. M. de Ruijter, P. M. van der Werf, and P. J. van Leeuwen, Institute for Marine and Atmospheric Research Utrecht, Department of Physics and Astronomy, Utrecht University, P.O. Box 80000, NL-3508 TA Utrecht, Netherlands.

H. Ridderinkhof, J. E. Ullgren, and H. M. van Aken, Department of Physical Oceanography, Royal Netherlands Institute for Sea Research, P.O. Box 59, NL-1790 AB Texel, Netherlands. (herman.ridderinkhof@nioz.nl)